



Available online at www.sciencedirect.com
jmr&t
 Journal of Materials Research and Technology
 journal homepage: www.elsevier.com/locate/jmrt



Original Article

Fundamental studies of magneto-optical borogermanate glasses and derived optical fibers containing Tb³⁺



Douglas F. Franco ^{a,**}, Roger G. Fernandes ^a, Jorlandio F. Felix ^b,
 Valmor R. Mastelaro ^c, Hellmut Eckert ^c, Conrado R.M. Afonso ^d,
 Younès Messaddeq ^{a,e}, Sandra H. Messaddeq ^e, Steeve Morency ^e,
 Marcelo Nalin ^{a,*}

^a Institute of Chemistry, São Paulo State University — UNESP, 14801-970, Araraquara, SP, Brazil

^b Institute of Physics, Applied Physics Center, University of Brasília, Brasília, DF, 70919-970, Brazil

^c São Carlos Institute of Physics, São Paulo University USP, 13566-590, São Carlos, SP, Brazil

^d Department of Materials Engineering (DEMa), Federal University of São Carlos - UFSCar, 13565-905, São Carlos, SP, Brazil

^e Centre d'Optique, Photonique et Laser, Université Laval, Quebec, Quebec, G1V 0A6, Canada

ARTICLE INFO

Article history:

Received 8 October 2020

Accepted 4 January 2021

Available online 13 January 2021

Keywords:

Magneto-optical glasses

Verdet constant

Faraday rotation

Optical fibers

ABSTRACT

New magnetic glass compositions, based on system (100-x) (60GeO₂ - 25B₂O₃ - 4Al₂O₃ - 10Na₂O - 1PbO) - xTb₄O₇ were prepared by the melt-quenching technique. The materials were systematically characterized with respect to their structural (XRD, EXAFS, XANES and Raman), thermal (DSC), morphological, optical, magnetic and magneto-optical (MO) properties. Morphological and magnetic measurements show the homogeneous distribution of the Tb³⁺ ions as the magnetic susceptibility increases proportionally to the rare earth content. The optical window covers the range from 0.5 up to 1.6 μm, limited by absorption due to 4f⁸ -> 4f⁷ 5d¹ and 4f⁸ -> 4f⁸ transitions of Tb³⁺. XANES and EXAFS measurements at the Ge-K edge show that the germanium atoms are always tetrahedrally coordinated, while results at the Tb-L_{III} edge shows terbium atoms to be eight-coordinated and exclusively present in the oxidation state 3+ independently of the glass composition. MO measurements show that the Verdet constant (V_B) increases linearly with the Tb³⁺ concentration reaching the value of -83.9 rad T⁻¹m⁻¹ at 650 nm for glass containing 8 mol % of Tb₄O₇. Good thermal stability (ΔT = 200 °C) allowed obtaining an optical fiber of a glass containing 4 mol% of Tb₄O₇ featuring V_B values of -37.9, -23.6 and -5.89 rad T⁻¹m⁻¹, at 500, 650 and 1550 nm, respectively.

© 2021 The Author(s). Published by Elsevier B.V. This is an open access article under the CC BY-NC-ND license (<http://creativecommons.org/licenses/by-nc-nd/4.0/>).

* Corresponding author.

** Corresponding author.

E-mail addresses: dffrancopdoctor@outlook.com (D.F. Franco), marcelo.nalin@unesp.br (M. Nalin).

<https://doi.org/10.1016/j.jmrt.2021.01.010>

2238-7854/© 2021 The Author(s). Published by Elsevier B.V. This is an open access article under the CC BY-NC-ND license (<http://creativecommons.org/licenses/by-nc-nd/4.0/>).

1. Introduction

During the past decades, novel glass compositions have revolutionized the scientific world by their countless technological applications [1–3]. Compositional tailoring glass properties towards special applications remains a goal that keeps inspiring scientists all over the world. During the past few years, strongly paramagnetic glasses have come into focus, motivated by the development of optical isolators, modulators, optical circulators, information storage devices and magneto-optical fiber sensors [4–8].

Magneto-optical (MO) glasses exploit the Faraday effect, i.e. the change in the plane of polarization in magnetic fields applied along the propagation direction [9]. One of the most important conditions for the optimization of Faraday effect in glasses is the incorporation of a high concentration of paramagnetic species, such as some transition metal and rare earth (RE) ions [9,10]. Among the RE elements, Tb^{3+} ions have attracted particular interest because they present one of the highest magnetic moments (total magnetic moment $J = L + S = 3 + 3$) among all lanthanides [9,11], and possess favorable optical properties, owing to the green ($^5\text{D}_4 \rightarrow ^7\text{F}_5$) emission near 544 nm. Indeed, Tb^{3+} -doped glasses have been reported in the literature as promising materials that present the largest Verdet constant values [9]. It is possible to prepare MO glasses containing high contents of Tb^{3+} , such borates, silicates, borogermanates, fluorophosphates and borosilicates with Verdet constant (V_B) values up to $-245 \text{ rad T}^{-1}\text{m}^{-1}$ at 632.8 nm [9,17–20].

Many works in the literature show that RE ions in heavy metal oxide (HMO) glasses usually induce structural changes in the glass network and, consequently modify some inherent characteristics, such as electrical, optical, spectroscopic and magnetic properties, which can lead to new applications [12–14]. It is essential to understand the structural modifications caused by the presence of RE ions in glasses in order to improve their desired properties [15,16]. A large number of MO materials based on glasses and crystals have been reported and are in use [21,22]. The best-known crystalline materials are the terbium aluminum garnet ($\text{Tb}_3\text{Al}_5\text{O}_{13}$ or TAG) with a V_B value near $-174 \text{ rad T}^{-1}\text{m}^{-1}$ (at 632 nm) [23] and terbium gallium garnet single crystals ($\text{Tb}_3\text{Ga}_5\text{O}_{12}$ or TGG) presenting V_B around $-134 \text{ rad T}^{-1}\text{m}^{-1}$ (at 632.8 nm) [24]. Recently, the number of works dedicated to the studies of MO glasses and glass-ceramics has been increasing significantly [25,26]. For example, Dai et al. [27] studied the synthesis and the magneto-optical property of TAG transparent glass-ceramics and showed that TAG crystals are homogeneously distributed in the glassy matrix. The Verdet constant of TAG glass-ceramic was found to be comparable to that of TAG single crystals.

According to Chen et al. [28] the V_B values in a single crystal are, in general, higher than for MO glasses. However, this disadvantage may be compensated by the possibility to prepare MO materials in a fiber form, since the Faraday rotation angle (θ) is proportional to the optical path length [29,30]. For this reason, developing new thermally stable magnetic glass matrices that do not crystallize during fiber production becomes an important objective. In this respect, HMO glasses

containing RE ions are attractive candidates because they exhibit properties such as, low phonon energy, high polarizability, and high refractive index [31–34]. Borogermanate glasses containing HMO have been intensively studied in this regard, mainly for the production of magnetic glasses containing high concentrations of paramagnetic species [9,35]. Gao et al. [9] showed that Tb^{3+} -doped $\text{GeO}_2\text{-B}_2\text{O}_3\text{-Al}_2\text{O}_3\text{-Ga}_2\text{O}_3$ (GBAG-Tb) glasses are potential candidates for solid-state lasers and optical fibers. When doped with high concentrations of Tb_2O_3 ($x = 14\text{--}25$ in mol%), MO glasses were realized having Verdet constant values between -48 and $-119 \text{ rad T}^{-1}\text{m}^{-1}$ (at 632.8 nm).

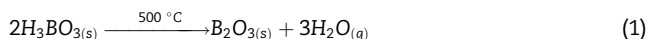
Magneto-optical fibers have been attracting attention for the development of modulators and optical isolators, current transducers, magnetic field sensors among other devices [36–39]. Many works propose the use of the MO fiber in the near infrared region. Ballato and Snitzer [40] reported the V_B value of a silicate fiber containing 54 wt% of Tb_2O_3 equal to $-20 \text{ rad T}^{-1}\text{m}^{-1}$ at $1.06 \mu\text{m}$. Cruz et al. [41] reported the V_B values in the range of 458–1523 nm for core-cladding silicate fibers consisting of a core (Ge:SiO_2) and a SiO_2 cladding. Notably, the V_B values reported at 633 and 1523 nm were 3.25 and $0.54 \text{ rad T}^{-1}\text{m}^{-1}$, respectively. In this study, we present the synthesis and characterization of a new magnetic Tb^{3+} -doped HMO borogermanate glass suitable for fiber production. The structural, thermal, morphological and spectroscopic properties were characterized by X-ray diffraction (XRD), differential scanning calorimetry (DSC), density analyses, high-resolution transmission electron microscopy (HRTEM), energy dispersive spectral analysis (EDS), X-ray absorption (XANES and EXAFS) spectroscopy, Raman and ultraviolet–visible (UV–vis) spectroscopies and refractive index measurements. In addition, we report the magnetic susceptibilities and the magneto-optical properties of the glasses and fibers via Faraday rotation experiment at different wavelengths.

Despite the considerable recent interest in magneto-optical glasses few works exist reporting their systematic structural exploration [9,17,42]. For example, the potential role of nano-scale-crystallization has often gone unexplored. Thus in the present study, special attention will be paid to the issue of the nano-structural arrangements.

2. Experimental

2.1. Bulk glass preparation

10-g batches of $(100-x)$ $(60\text{GeO}_2\text{-}25\text{B}_2\text{O}_3\text{-}4\text{Al}_2\text{O}_3\text{-}10\text{Na}_2\text{O-}1\text{PbO-}x\text{Tb}_4\text{O}_7)$ (GBANPb- x Tb or x Tb) glassy samples were prepared by the melt-quenching method, using chemical grade germanium oxide, GeO_2 (Sigma–Aldrich), boric acid H_3BO_3 (Sigma–Aldrich), aluminum oxide Al_2O_3 (Sigma–Aldrich), sodium carbonate Na_2CO_3 (Sigma–Aldrich), lead oxide PbO (Sigma–Aldrich) and terbium oxide Tb_4O_7 (Sigma–Aldrich). Vitreous boron oxide was obtained by thermal decomposition of $2\text{H}_3\text{BO}_3$ at 500°C for 30 min in an electric furnace, according to the chemical reaction shown below in Eq. (1):



The resulting material was the mixed with the other ingredients and finely ground to powder, homogenized in a speed mixer using a Flacktek equipment and melted in a platinum crucible at 1400 °C for 2 h under atmospheric conditions. The melt was cooled into a stainless-steel mold preheated at 30 °C below the glass transition temperature (T_g) for each glass composition and annealed for 2 h to minimize thermal stress. Finally, the sample was cooled to room temperature (RT) at a rate of 0.5 °C.min⁻¹, resulting in light-yellow glasses of approximately 2.5 mm thickness and 1.7 cm of length. All the samples were polished using silicon carbide (SiC) polishing paper to reach optical quality.

2.2. Glass preform preparation and fiber drawing

Initially, the main point to ensure a good quality of the optical fiber is the step of glass preform preparation. In this work, the 96(60GeO₂-25B₂O₃-4Al₂O₃-10Na₂O-1PbO)-4Tb₄O₇ glass (GBANPb-4Tb) was chosen for the fiber drawing process. This composition presented the highest thermal stability parameter ($\Delta T = 290$ °C) against devitrification ensuring the successful production of transparent fibers free from crystalline inclusions.

In the first step, a 40 g glass rod was prepared by the melt-quenching/annealing method, using the procedure described above. To obtain a good preform surface quality, the preform was polished in different steps using SiC paper from 600 to 4000 mesh. Afterwards, the glass rod was manually inserted into a silica glass tube and the assembly was mounted into the heating zone of the fiber drawing tower furnace under N₂ atmosphere. Initially, the temperature of the furnace was raised to 525 °C (T_g) using a heating rate of 50 °C min⁻¹ and, subsequently, the temperature was increased to 650 °C ($T_g + 125$ °C) to the beginning of the fiber drawing process. During the drawing process, the fiber was coated with low-index UV-cured– polymethylmethacrylate, to protect and improve its mechanical resistance. The fiber diameter was 125 µm, as measured by a Leica DM2500M microscope using an objective lens of 100×.

2.3. Characterization techniques

Differential scanning calorimetry (DSC) measurements were carried out in a Netzsch DSC 404 F3 Pegasus calorimeter, from 300 to 1000 °C, at a heating rate of 10 °C.min⁻¹, under nitrogen atmosphere (20 mL min⁻¹) in platinum crucibles.

X-ray powder diffraction experiments were carried out in a Bruker D8 Advance diffractometer operating with a Ni-filtered CuK α radiation source, at 2 θ angles ranging from 10 to 80° in 0.01° steps of 1 s.

HRTEM images and SAED patterns were obtained from powdered glasses, suspended in ethanol and deposited on copper grids in a FEI Model Tecnai G² F20 (200 kV) transmission electron microscope with a field emission gun and coupled energy dispersive spectroscopy (EDS) microanalysis.

X-ray absorption near-edge structure (XANES) and extended X-ray absorption fine structure (EXAFS) spectra of

GBANPb-xTb glasses and the crystalline reference samples, germanium (IV) oxide (rutile phase), Tb₂O₃ and Tb₄O₇ were collected at the XAFS2 beamline at the Brazilian National Synchrotron Light Laboratory (LNLS, Brazil) at the Ge K-edge (11,113 eV) and the Tb-L_{III} absorption edge (7514 eV) at RT. The glasses were finely powdered in an agate mortar and dispersed in boron nitride (BN) to prepare pellets with a specific thickness for the analyses. Subsequently, the mixtures were pressed into pellets of around 1 mm thickness, which were then fixed between two Kapton adhesive tapes and attached to the X-Ray beamline. For comparison purposes the background signals of all EXAFS spectra were removed and intensities normalized to the amplitude of the signal corresponding to first coordination shell around 1.74 Å for Ge and 1.86 Å for Tb. The normalization of the XANES spectrum was done using the software available at the Multiplatform Applications for XAFS code (MAX) [43,44].

EXAFS spectra at Ge K-edge and Tb L_{III}-edge were collected using 1 eV around the edge and 2 eV beyond the edge with an acquisition time of 2 s per point for all the ranges. A k-range from 1.8 to 12.8 Å⁻¹ was selected for the calculation of the Fourier transform. For the fitting of the contribution of the first coordination shell around Ge and Tb atoms, the inverse Fourier transforms were calculated (graphs not shown). The filtered EXAFS spectra, obtained with the inverse Fourier transform, were processed using the Multiplatform Applications for XAFS code (MAX) with the amplitude and phase shift functions being calculated using the FEFF8.2 ab initio code [43,44].

The density analyses of GBANPb-xTb samples were performed using a Mettler Toledo Excellence XS densimeter according to the Archimedes principle. The measurement precision was 0.002 g cm⁻³.

Raman spectra were recorded at RT in a frequency range from 200 to 1500 cm⁻¹ in a HORIBA Jobin Yvon model LabRAM HR micro Raman apparatus equipped with a 632.8 nm laser, delivering 17 mW.

Optical absorption and transmission spectra of GBANPb-xTb glasses were obtained by using a Varian Cary 5000 UV–Vis–near infrared (NIR) spectrophotometer, in a spectral range from 300 to 600 nm and from 300 to 2000 nm, respectively.

Linear refractive indices for the GBANPb-xTb (x = 4, 6 and 8) glasses were measured by using the prism coupling technique via M-Lines Metricon 2010 equipment at 532, 633, 972, 1038 and 1538 nm with a precision of ±0.001.

Emission spectra on the bulk glass samples were obtained at RT on a Fluorolog Horiba Jobin Yvon fluorimeter, using an excitation wavelength of 377 nm and slit widths of 1 mm.

Magnetization measurements were done using a VSM-SQUID from Quantum Design PPMS3 with a DC field ranging from -70 to 70 kOe and temperatures ranging from 5 to 300 K. Temperature-dependent magnetic susceptibilities were studied under a magnetic field of 30 Oe and temperature ranging from 5 to 300 K. The diamagnetic correction was done from the undoped GBANPb (0 Tb) glass.

Faraday rotation angles (θ) of GBANPb-xTb glasses (where x = 4, 6 and 8) were measured at RT using an optical setup containing a permanent NdFeB magnet of dimensions 6x7x7 cm. In the center of the magnet, there is a circular orifice

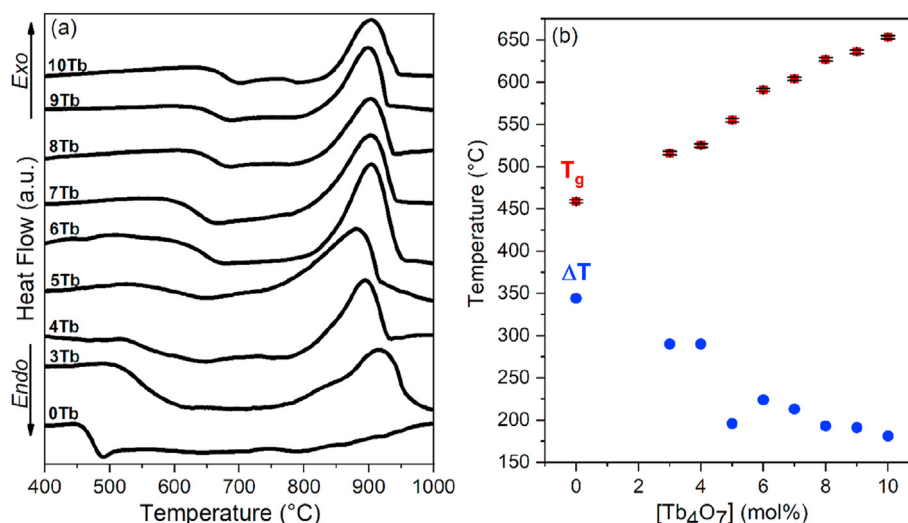


Fig. 1 – (a) DSC curves and (b) Evolution of T_g and ΔT as a function of the content of Tb_4O_7 .

with 1.5 cm diameter and 4.5 cm of the optical path with a fixed magnetic field of 0.46 T. The Faraday rotation setup was calibrated using a commercial terbium gallium garnet (TGG) single crystal with a length of 20 and 4 mm of diameter from MolTech GmbH, with a V_B value of $-129 \text{ rad T}^{-1} \text{ m}^{-1}$.

The Faraday rotation measurements were performed at different wavelengths, i.e. 500, 650, 880, 1050, 1330 and 1550 nm using a Superk Compact Supercontinuum laser with an optical spectral range of 450–2400 nm, a total output power of 100 mW and operation temperature range of 15–30 °C. Bulk glasses had their optical path lengths standardized around 1.7 cm. The samples were polished to obtain flat surfaces. The Faraday rotation angle for GBANPb-4Tb glass fiber was obtained in a fiber piece of 10 cm length. The optical path length within the 0.46 T magnet was $l = 4.5 \text{ cm}$.

Before insertion, the fiber was cleaved on the input and output edges using a cleaving machine 24X0-RCL optimized for fiber of 125 μm diameter. The fiber was attached in a holder and the laser was focused on the fiber using an objective lens of 40 \times . The polarized light transmitted through the samples had their Faraday rotation measured in quadruplicate by a graduated polarizer with a precision of 2°. The output beams at 500, 650, 880 and 1050 nm were detected using a photodetector model PM100D Firmware V2.32 Handheld Optical Power and at 1330 and 1550 nm using a PDA015C InGaAs Fixed Gain Amplified Detector connected to a BK Precision 2512 100 MHz 1 GSa/s Handheld Digital Storage Oscilloscope. The Verdet constant values (in $\text{rad T}^{-1} \text{ m}^{-1}$) were calculated according to the Faraday rotation equation (see Section 5.2).

3. Results and discussion

The results of this study are presented in three principal parts. The first one reports the fundamental properties of the glass and its short and long range order structural analysis. The second part focuses on the magnetic, optical and magneto-

optical properties of the system while the third part reports the magneto-optical fiber properties. During the study of the glass compositions in this work, we observed that all samples were attracted by a commercial Nd-based magnet (N42 grade, with a magnetic field estimated at 1.32 T). The force of the magnetic attraction increases with increasing Tb^{3+} content (see graphical abstract).

3.1. Thermal properties

Fig. 1a shows the DSC curves, from which the glass transition temperature (T_g) and the onset of crystallization temperature (T_x) were obtained and used to estimate the thermal stability parameter ($\Delta T = T_x - T_g$). ΔT is a useful parameter for the choice of the glass composition to be used in magneto-optical fiber preparation. Table 1 summarizes the T_g , T_x and ΔT values for all samples (estimated errors are $\pm 2 \text{ }^\circ\text{C}$ for T_g and $\pm 4 \text{ }^\circ\text{C}$ for ΔT).

As it can be seen from both Table 1 and Fig. 1b, the T_g values increase progressively as a function of the concentration of Tb^{3+} ions in the GBANPb matrix, varying from 530 °C (in GBANPb-3Tb) to 655 °C (in GBANPb-10Tb). The ΔT parameter presented a maximum value around 344 °C for the sample

Table 1 – Characteristic temperatures, glass transition (T_g), onset of crystallization (T_x) and thermal stability parameter (ΔT) for all analyzed samples.

Samples	T_g ($\pm 2 \text{ }^\circ\text{C}$)	T_x ($\pm 2 \text{ }^\circ\text{C}$)	ΔT
GBANPb-0Tb	459	803	344
GBANPb-3Tb	516	806	290
GBANPb-4Tb	525	815	290
GBANPb-5Tb	555	751	196
GBANPb-6Tb	591	815	224
GBANPb-7Tb	604	817	213
GBANPb-8Tb	627	820	193
GBANPb-9Tb	636	827	191
GBANPb-10Tb	653	834	181

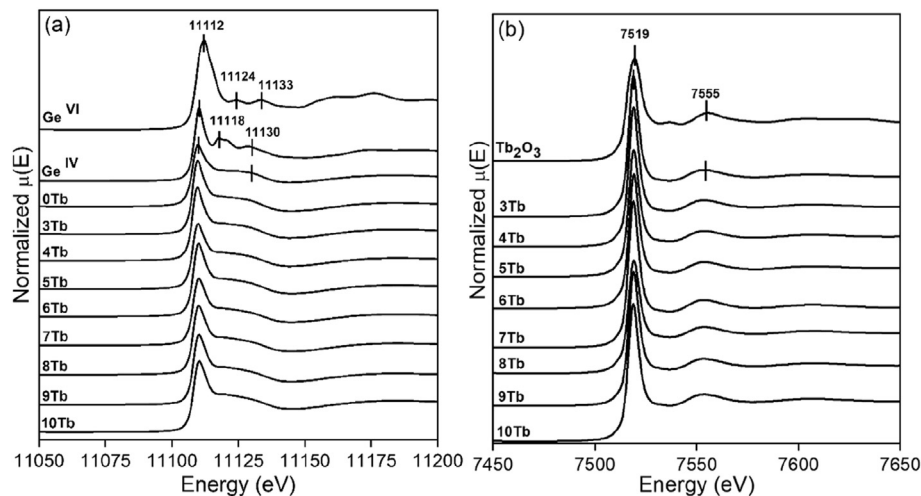


Fig. 2 – (a) Ge K-edge and (b) Tb L_{III}-edge XANES spectra of the GBANPb-xTb glasses and reference compounds.

without Tb and decreases continuously as the amount of Tb increases, reaching 181 °C for GBANPb-10Tb sample. It is interesting to notice that despite the changes in T_g , the temperatures of the crystallization peaks (T_p) do not change significantly. The increase of T_g as a function of the Tb content suggests structural changes leading to higher rigidity of the glassy skeleton and is in agreement with the structural model proposed by Yamashita et al. [45]. Tb_4O_7 can be considered as a modifier agent of the vitreous network. The structural origins of the increase in T_g with increasing network modifier concentration will be addressed below on the basis of the spectroscopic investigations.

3.2. Structural properties: XRD, XANES, EXAFS and Raman spectroscopy characterization

3.2.1. X-ray diffraction

XRD patterns of GBANPb-xTb glasses are shown in Fig. SM1 (supporting information). All samples exhibit the halo, characteristic of non-crystalline materials and together with the T_g confirm the macroscopically vitreous nature of the GBANPb samples and the absence of any crystalline component. As observed on Fig. SM1, the sample without Tb presents the halo at 2θ equal to 23° and a shift towards higher angles can be noted as the Tb content increases.

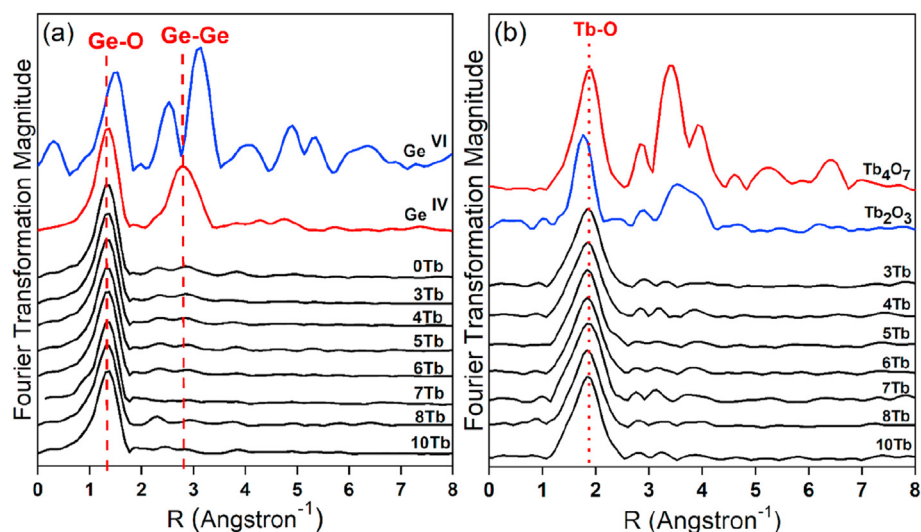


Fig. 3 – (a) Fourier transformed EXAFS signals for the GBANPb-xTb glasses compared to the GeO_2 reference compounds with Ge coordination numbers four and six and (b) Fourier transformed EXAFS signals for the GBANPb-xTb glasses compared to those of the Tb_2O_3 and Tb_4O_7 standards.

Table 2 – Structural parameters obtained from the fitting of the EXAFS data corresponding to the first coordination shell around Ge atoms of GBANPb-xTb glasses and GeO₂ tetragonal reference compound. N = Ge–O coordination number, R = Ge–O bond-length, σ = Debye-Waller factor, ΔE = Energy shift, QF = Fitting quality factor.

Bond	Samples	N	R (Å)	$\sigma^2_{\text{Ge-O}} (10^{-3})$	ΔE (eV)	QF
Ge–O	GeO ₂ tetragonal	4*	1.734 ± 0.004	2.8 ± 0.0004	1.2 ± 0.5	74
Ge–O	GBANPb-3Tb	4.2 ± 0.2	1.744 ± 0.004	3.6 ± 0.0003	0.8 ± 0.4	1.5
Ge–O	GBANPb-4Tb	4.2 ± 0.2	1.745 ± 0.005	4.1 ± 0.0004	0.8 ± 0.5	1.3
Ge–O	GBANPb-5Tb	4.2 ± 0.2	1.745 ± 0.005	4.3 ± 0.0003	0.9 ± 0.4	1.1
Ge–O	GBANPb-6Tb	4.2 ± 0.2	1.747 ± 0.005	4.1 ± 0.0004	0.9 ± 0.5	1.6
Ge–O	GBANPb-7Tb	4.2 ± 0.2	1.744 ± 0.006	4.3 ± 0.0004	0.5 ± 0.5	2.0
Ge–O	GBANPb-8Tb	4.2 ± 0.2	1.747 ± 0.005	5.9 ± 0.0005	0.8 ± 0.4	1.0
Ge–O	GBANPb-10Tb	4.2 ± 0.2	1.749 ± 0.005	4.5 ± 0.0004	0.9 ± 0.5	1.7

3.2.2. Short-range order: XANES and EXAFS

Fig. 2a shows the normalized XANES spectra for Ge K-edge of GBANPb-xTb glasses, and the crystalline reference compounds α -quartz-type GeO₂ [four-coordinated Ge] and rutile-GeO₂ [six-coordinated Ge]. The reference compound comparison strongly suggests that the germanium atoms are in a tetrahedral environment in all the glass samples.

Fig. 2b presents the comparison between the normalized Tb L_{III}-edge XANES spectra of the GBANPb-xTb glasses and the Tb₂O₃ reference sample. The XANES spectrum of Tb₄O₇ was previously measured by Potdevin et al. [46]. It presents a splitting of the absorption edge peak, resulting in two shoulders around 7520 and 7528 eV, indicating the distinct responses of the two different oxidation states, Tb³⁺ and Tb⁴⁺, respectively [46]. In contrast, the glasses show their absorption edges around at 7518 eV assigned to the Tb³⁺ ions, closely resembling the result obtained for Tb₂O₃ (Fig. 2b). Thus, although the glasses had been prepared with mixed-valent Tb₄O₇, we conclude that their melting conditions result in the exclusive presence of Tb³⁺.

Fig. 3a and 3b shows the EXAFS spectra of glasses and reference samples collected at the Ge–K and Tb–L_{III}-edges allowed obtaining quantitative information about the local environment around Ge and Tb atoms.

From the analysis of EXAFS Fourier transforms, the first peak around 1.734–1.747 Å could be assigned to the Ge–O first coordination shell, Fig. 3a [47,48]. Consistent with the conclusion from the XANES data the EXAFS spectra indicate four-coordinated Ge atoms in all the samples. The data give no evidence of Ge–O distances involving non-bridging oxygen atoms.

The Tb–L_{III} EXAFS spectra of glasses present a peak around 2.29 Å assigned to the Tb–O distances of the first coordination shell of Tb atoms like those observed for Tb₂O₃ reference compound [49,50]. The structural parameters extracted from the fitting of the EXAFS data corresponding to the first coordination shell around Ge and Tb atoms are summarized in Tables 2 and 3.

According to the EXAFS fitting results presented in Table 2, the Ge coordination number (N) for all studied glasses is 4 and is similar to the Ge local structure in vitreous and tetragonal GeO₂, consistent with a random network of corner-shared GeO₄ units [48,51].

The increase of Tb₄O₇ concentration does not induce significant modifications to the Ge–O distance and to the Debye-Waller factor, meaning that the local environment around the Ge atoms remains essentially unaffected by the presence of terbium oxide.

The Tb–O inter-atomic (R_M) distance values for all glasses are shown in Table 3. The coordination number (N) of the first shell indicates the presence of eight oxygen atoms around the Tb ions. According to Bowron et al. [49] the data suggests a mixture of pseudooctahedral and body-centered cubic geometry for the RE ions. As observed for Ge, the Tb–O distances and the Debye-Waller factors remain constant, showing no change in the structural role of Tb³⁺ as their concentration in the glass increases.

3.2.3. Raman spectroscopy

In terms of Raman spectroscopic data, it will be necessary to highlight some general spectral characteristics of borogermanate glasses containing high concentrations of

Table 3 – Structural parameters obtained from the fitting of the EXAFS spectra corresponding to the first coordination shell around Tb atoms of GBANPb-xTb glasses and Tb₂O₃ reference compound. N = Tb–O coordination number, R = Tb–O bond-length, σ = Debye-Waller factor, ΔE = Energy shift, QF = Fitting quality factor.

Bond	Samples	N	R (Å)	$\sigma^2_{\text{Tb-O}} (10^{-3})$	ΔE (eV)	QF
Tb–O	Tb ₂ O ₃	8*	2.27 ± 0.01	0.0092 ± 0.0008	1.4 ± 0.4	42
Tb–O	GBANPb-3Tb	8.4 ± 0.6	2.29 ± 0.01	0.015 ± 0.002	0.9 ± 0.3	1.4
Tb–O	GBANPb-4Tb	8.4 ± 0.5	2.29 ± 0.01	0.016 ± 0.002	0.9 ± 0.2	1.2
Tb–O	GBANPb-5Tb	8.2 ± 0.5	2.29 ± 0.01	0.016 ± 0.001	1.0 ± 0.3	1.0
Tb–O	GBANPb-6Tb	8.0 ± 0.1	2.29 ± 0.01	0.016 ± 0.001	1.0 ± 0.3	1.0
Tb–O	GBANPb-7Tb	8.6 ± 0.6	2.29 ± 0.01	0.015 ± 0.001	1.0 ± 0.3	1.6
Tb–O	GBANPb-8Tb	8.0 ± 1.5	2.29 ± 0.01	0.016 ± 0.001	1.0 ± 0.3	0.7
Tb–O	GBANPb-10Tb	8.7 ± 0.5	2.29 ± 0.01	0.014 ± 0.001	1.3 ± 0.3	0.8

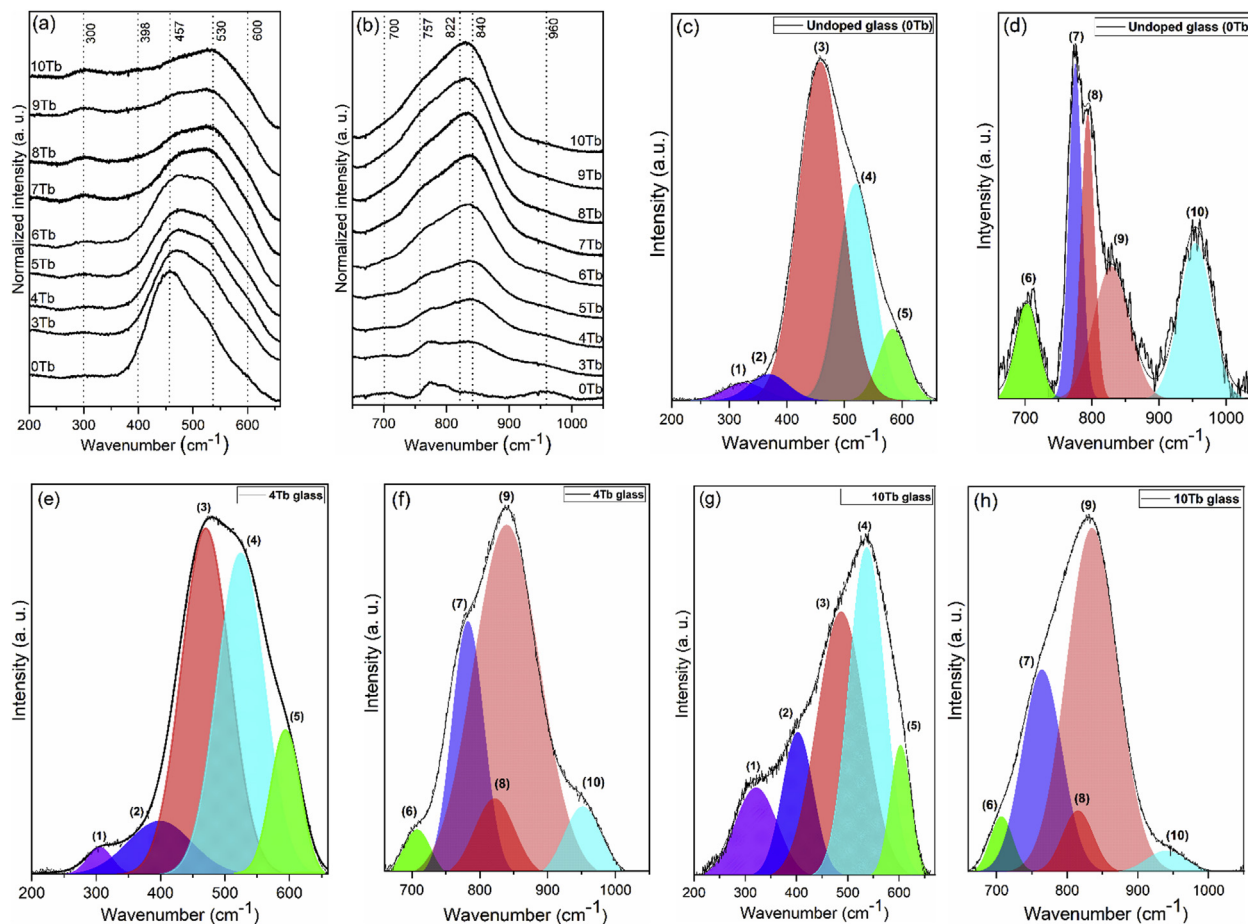


Fig. 4 – (a–b) Normalized Raman spectra of the GBANPb- x Tb, in which ($x = 0; 3; 4; 5; 6; 7; 8; 9$ and 10 mol% of Tb_4O_7) in the ($200\text{--}660\text{ cm}^{-1}$) and ($660\text{--}1050\text{ cm}^{-1}$) ranges, respectively. Deconvolution of the Raman spectra of the glass samples (c–d) 0 Tb, (e–f) 4 Tb and (g–h) 10 Tb.

modifying oxides on the glassy network [52–56]. In the literature, some works report that physical properties of alkali germanate glasses, such as their densities, glass transition temperatures, and refractive indices are strongly influenced by a phenomenon called the germanate anomaly and there are different structural propositions to explain such behavior [54,57]. In one of them, Ianov and Evstropiev [15] reported that the anomaly is the result of the conversion of germanium ions from four-fold to six-fold ($GeO_4 \rightarrow GeO_6$) coordination upon the addition of network modifiers. Alternatively, Henderson and Fleet [57] propose the formation of three-membered rings, involving distorted $[GeO_4]$ tetrahedral.

Fig. SM2a summarizes the Raman spectra of all GBANPb- x Tb glasses analyzed. Consistent with our X-ray Absorption data, we find no evidence of vibrational modes that could be assigned to the presence of GeO_6 groups. To better understand the changes, the Raman spectra were divided in two regions denominated I and II in which the main evidences of structural changes in the glass network can be observed (Fig. 4a and b).

Fig. 4c–4h shows the deconvoluted Raman spectra of GBANPb- x Tb glasses ($x = 0, 4$ and 10) in those two spectral

regions, respectively. These figures include a deconvolution of these spectra into ten symmetrical Gaussian components, following previous works on borogermanate, borate and germanate glasses [16,52,54,58–64]. Raman spectra of GeO_2 and B_2O_3 glassy phases and for the crystalline compounds are presented in the supporting information section (Fig. SM2b).

The low frequency (region I) is dominated by an intense broad band typical of glasses containing higher concentrations of GeO_2 . The Raman spectrum of the undoped GBANPb (0 Tb) glass shows a weak broad band around 300 cm^{-1} and a much more intense band near 457 cm^{-1} , besides three shoulders around at $398, 530$ and 600 cm^{-1} , Fig. 4a–b [58,63]. This spectral profile was observed in the Raman spectra of all three glasses (0, 4 and 10 Tb) and from the deconvolution process, it was possible to obtain more details about the contributions of the vibrational modes of germanium and boron in the glass network (Fig. 4c, e and g). The peaks fitted are equivalents in terms of assignments of vibrational modes, but differ in shape, band intensities and frequency with the increase of Tb_4O_7 .

In terms of assignments, Rivera et al. [55] and Kamitsos et al. [59] suggest that the region between 300 and 500 cm^{-1}

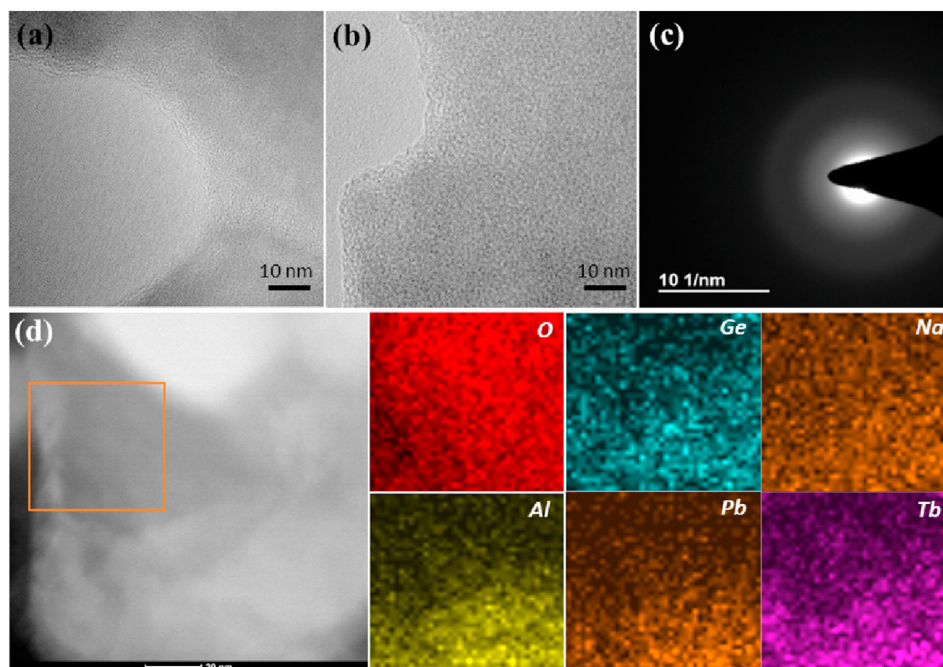


Fig. 5 – HRTEM micrographs of (a) GBANPb-4Tb and (b) GBANPb-6Tb glasses, (c) SAED pattern of the GBANPb-6Tb sample and (d) SEM-EDS elemental mapping of GBANP-4Tb₄O₇ glass.

(peaks 1 and 2) are dominated by Ge–O bending modes. The peak (I) at 306 cm^{-1} is assigned to deformation vibrations of Ge atoms in the glassy network [55,58,59], while peaks (2) and (3) at 397 and 470 cm^{-1} refer to the vibrations of B–O–B bonds and symmetric stretching vibrations of Ge(IV)–O–Ge(IV) bonds in 4-membered GeO_4 rings, respectively. Peaks (4) and (5) at 524 and 594 cm^{-1} are assigned to the deformation modes of Ge(IV)–O–Ge(IV) corresponding to the transversal (TO) and longitudinal (LO) split (Fig. 4c, e and g), [16,52,55,58,64].

In this case, it is important to highlight that the increase of the Tb^{3+} ions concentration leads to a decrease of the intensity of its broad band centered around 457 cm^{-1} in GBANPb-0Tb, suggesting a decrease of the number of oscillators referring to symmetric stretching of Ge–O–Ge bonds, possibly due to depolymerization of the Ge–O–Ge linkages decreasing the fraction of bridging oxygen species (BO), Fig. 4a.

In region I, two significant spectroscopic changes can be highlighted with increasing Tb_4O_7 content: (i) the decrease in intensity of the broad band centered at 457 cm^{-1} (0 Tb glass) and (ii) a shift of the broad band at 457 cm^{-1} (0 Tb glass) to higher wavenumbers, e.g. to 523 cm^{-1} (10 Tb glass), Fig. 4a. Following Rivera's [55] assignment of the bands around 453 and 532 cm^{-1} to the symmetric stretching vibrations of Ge–O–Ge bonds associated with 4- and 3-membered GeO_4 rings, respectively, our data suggest a conversion of the 4-membered to 3-membered rings with the increase of Tb content (Fig. 4a).

In the medium frequency region (region II), the broad band between 660 and 1050 cm^{-1} comprises the response to vibrational modes of the borate and germanate networks with overlapping frequency ranges. In Fig. 4b, we can observe that with increasing Tb_4O_7 concentration the broad band in the

region II increases in intensity suggesting the breaking of Ge–O–Ge linkages to form Ge-O^- units [43,60,61]. This region is predominantly dominated by non-bridging oxygen (NBO) species bonded to germanium (Ge-O^- species) [52,55].

Figs. 4(d, g and h) shows the deconvolution of the GBANPb-xTb (0, 4 and 10 Tb) spectra in this frequency range. In this case, it was possible to identify five components (peaks 6–10) around 700 , 757 , 822 , 840 and 960 cm^{-1} [52,55,65,66]. Mansour et al. [54] and Henderson et al. [63] showed that the Raman spectra of germanate glasses containing different concentrations of network modifier agents present Raman bands between 700 and 950 cm^{-1} which can be attributed to Ge^2 and Ge^3 units (in the Q^n terminology the superscript “n” denotes the number of bridging oxygen atoms bound to a network former unit). The non-bridging oxygen atoms bound to these Ge^2 and Ge^3 units arise from network depolymerization of Ge–O–Ge linkages. In addition, B–O stretching modes associated with various borate ring structures contribute in this frequency region. Tentative assignments of these deconvolution components to individual network forming units were made by comparison with the spectra of binary alkali borate and germanate glasses. According to Koroleva et al. [52], the band around $700\text{--}740\text{ cm}^{-1}$ (peak 6) occurs in the region where the symmetrical stretching vibrations of metaborate chains is observed (Fig. 4d, g and h). In a similar vein the band at 782 (peak 7) cm^{-1} may be assigned to symmetrical stretching vibrations of borate rings (di-triborate rings) [52,54,60]. The band at 822 cm^{-1} (peak 8) may represent the symmetrical stretching vibrations of Ge–O $^-$ (NBO) in Ge^2 -species while that at 840 cm^{-1} (peak 9) could arise from that in Ge^3 - species [43,54]. Finally, the band at 951 cm^{-1} (peak 10) might be attributed to the vibrational mode of diborate groups (Fig. 4d, g and h), [52].

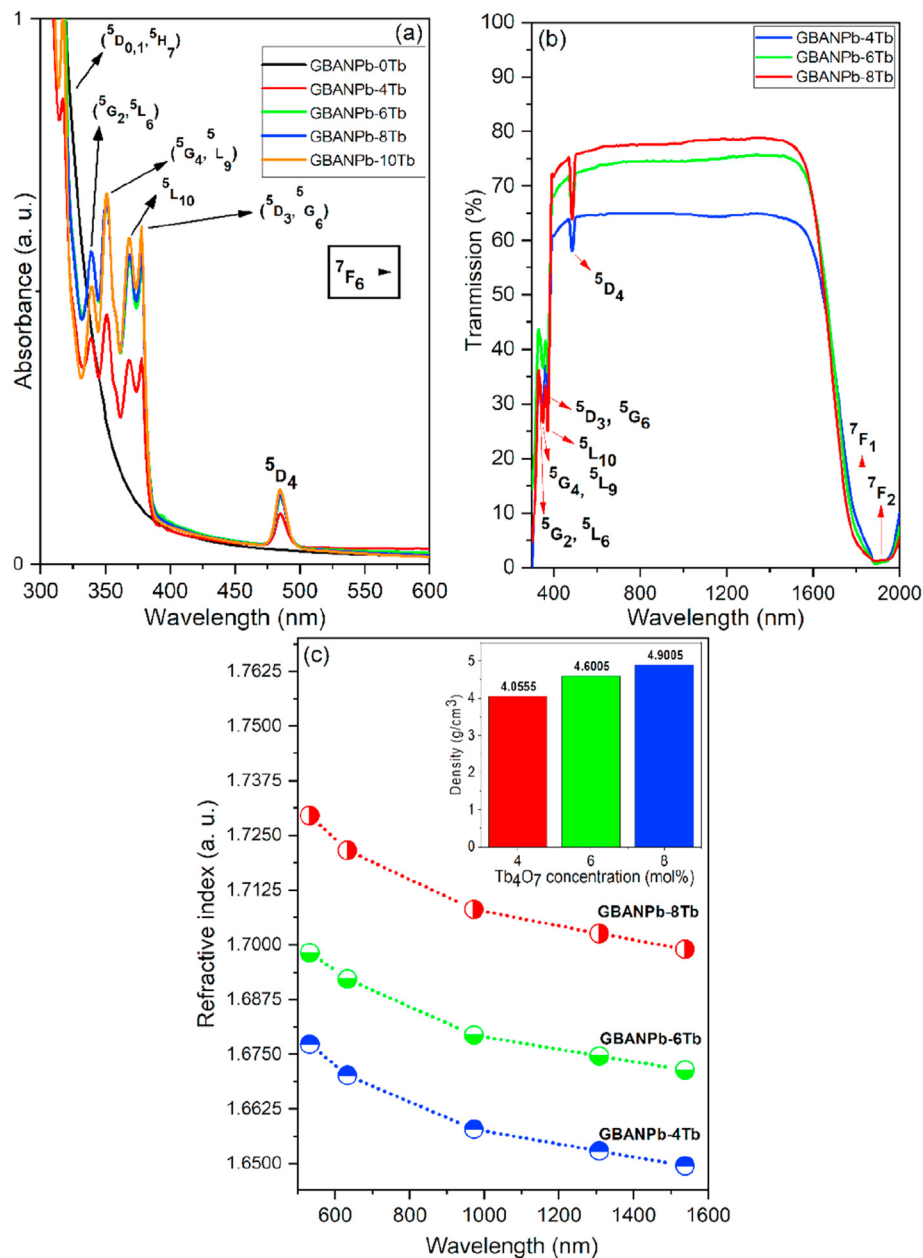


Fig. 6 – (a) UV–Vis absorption spectra of the GBANPb-xTb glasses (b) Normalized transmission spectra and (c) refractive indices at different wavelengths. Inset: density as a function of Tb₄O₇ concentration.

Figs. 4e-h, allow a detailed comparison of the GBANPb-4Tb and GBANPb-10Tb glass samples within regions I and II. In region I (200-660 cm⁻¹), in GBANP-10Tb spectrum, we note that the band near 488 cm⁻¹ (peak 3') and assigned to the symmetric stretching vibrations of Ge(IV)-O-Ge(IV) bonds in 4-membered GeO₄ rings, decreases in intensity with increasing Tb₄O₇ content, Fig. 4g [55]. This behavior reflects the proposed depolymerization of the glass network (decrease in the number of Ge(IV)-O-Ge(IV) linkages, accompanied by an increased contribution of vibrational modes involving NBO bonds in the middle region (660-1050 cm⁻¹) (Fig. 4h). Likewise, we can note an intensity attenuation of two shoulders at 707 (peak 6') and 942 cm⁻¹ (peak 10') assigned to the deformation

modes of Ge atoms in the glassy network and to the vibrational mode of diborate groups [52,58].

Also, an increased Tb₄O₇ content leads to a noticeable attenuation of the shoulder represented by the peak (7') at 764 cm⁻¹ assigned to the symmetrical stretching vibrations of borate rings (di-triborate rings) (Fig. 4h), [52]. In addition, we draw attention to the range between 810 and 900 cm⁻¹, peak (9') assigned to the stretching vibrations of NBO in Q³-species (GeO₄ with three bridging oxygen atoms) (Fig. 4h) [52,55,64].

In addition, for all glasses, above 1050 cm⁻¹, there is a broad band centered around 1400 cm⁻¹ and a shoulder at approximately 1320 cm⁻¹ (Fig. SM2a). Their wavenumbers coincide with those of the stretching vibrations of B-O bonds

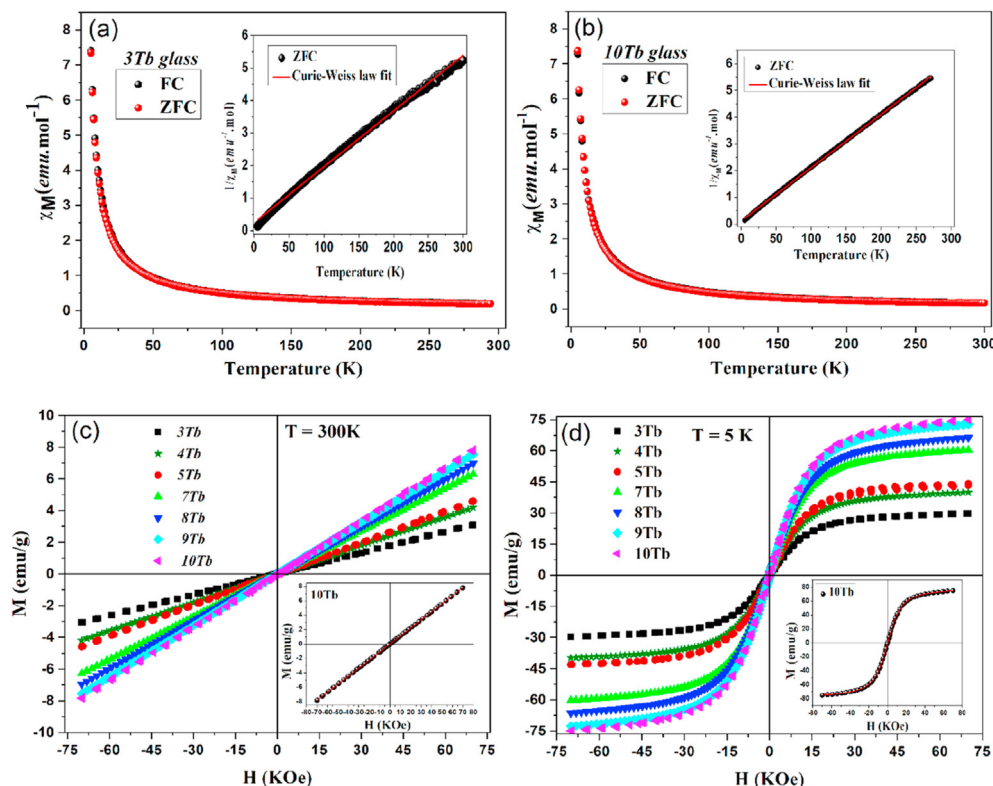


Fig. 7 – Temperature dependence (FC and ZFC) of the magnetic susceptibility χ_M at 30 Oe for glass doped with (a) 3 and (b) 10% of Tb_4O_7 . The inset shows the $1/\chi$ vs. T plot documenting the validity of the Curie–Weiss law in the temperature range from 5 to 300 K. (c) Magnetization versus field measured at 300 K for all GBANPb- x Tb glasses ($3 \leq x \leq 10$) and (d) analogous plot at 5 K. The insets show magnetization data plotted as a function of H , along with an empirical fit to a Brillouin function using the Tb^{3+} free ion g -value of 1.5.

of metaborate units within and outside of ring structures, respectively (Fig. SM2a) [52,67].

3.3. Morphological and chemical analysis: HRTEM and EDS mapping

Fig. 5a–5d shows the HR-TEM images and SEM-EDS mapping for two different vitreous compositions GBANPb-4Tb and GBANPb-6Tb, respectively. The High-Resolution images confirm the absence of clusters or crystals in the nano-scale, consistent with a homogeneous distribution of all elements (Fig. 5a-b).

The traditional (Bragg) X-ray diffraction technique is generally used for the characterization of the ordinary crystals with micrometric dimensions [68]. Crystals on the nano-scale may elude detection by this method, since their diffraction patterns may be broadened beyond detectability. This restriction is overcome by the use of electron diffraction (SAED), which is a crystallographic technique applied during the HR-TEM measurements.

Fig. 5c shows the SAED pattern for the GBANPb-6Tb glass composition. As expected from the HR-TEM data, no diffraction peaks were observed confirming the absence of nano-crystals and the absence of heterogeneity at this length scale. Fig. 5d shows the SEM-EDS map of GBANPb-4Tb glass,

suggesting a homogeneous distribution of its elemental constituents, see also Fig. SM3a-b.

4. Optical properties

Fig. 6a shows the UV–Vis absorption spectra of GBANPb- x Tb ($x = 0, 4, 6, 8$ and 10 mol%) glasses. The UV–Vis spectrum of the terbium-free glass ($x = 0$) shows that the absorption edge of the glassy matrix is close to 400 nm. The absorption edge is an important criterion for possible applications of glasses, such as optical cut-off light filters [69]. For the Tb containing samples we observe the Tb^{3+} 4f-4f absorption bands at 485, 378, 368, 351, 339, and 317 nm. They are assigned to the electronic transitions from the 7F_6 ground state to the excited states 5D_4 (5D_3 , 5G_6), $^5L_{10}$ (5G_4 , 5L_9) (5G_2 , 5L_6) and ($^5D_{0,1}$, 5H_7) [70].

Fig. 6b shows the transmittance spectra for three compositions, GBANPb- x Tb ($x = 4, 6$ and 8 mol%) in the range from 200 to 2000 nm. Besides the absorption bands limiting the transparency of glasses at higher energy, the optical windows are limited in the near infrared by the Tb^{3+} transitions ($^7F_6 \rightarrow ^7F_0$) and ($^7F_6 \rightarrow ^7F_1$) at 1850 and 1915 nm, respectively [71].

The refractive index values of GBANPb- x Tb ($x = 4, 6$ and 8 mol %) glasses as a function of wavelength in the visible and near-infrared regions are shown in Fig. 6c. For all analyzed wavelengths the refractive indices increase with increasing Tb_4O_7

concentration. As expected, the increase in refractive index is correlated with an increase in density (see inset of Fig. 6c. In addition, the increased concentration of NBO species with increasing terbium content may contribute to this trend [72].

Photoluminescence studies reveal strong quenching of Tb^{3+} emissions in the visible range at high Tb-concentration. More details about the emission curves together with life time results are shown in the supplementary materials and Fig. SM4a-b.

5. Magnetic properties

5.1. Magnetic susceptibility and magnetization studies

The magnetic properties of glasses doped with Tb have been investigated by measurements of magnetic susceptibility, over the temperature range of 5–300 K. Fig. 7a and 7b shows the temperature dependence of magnetic susceptibilities (χ_M) of glasses doped with 3 mol% (3 Tb) and 10 mol% (10 Tb) of Tb_4O_7 , respectively. The curves were modeled using the Curie–Weiss law (equation 2),

$$\chi_M = \frac{C}{T - \theta} \quad (2)$$

where C is the Curie constant, and θ is the Weiss temperature. In the inset of Fig. 7 is shown the inverse of susceptibility χ^{-1} vs temperature for zero-field cooling (ZFC) measurements (Field cooling results, not shown here, presented the same behavior). The linear correlation indicates that the magnetic response is adequately modeled using the Curie–Weiss law. The results indicate that both glasses doped with 3 and 10 mol % Tb_4O_7 exhibit a paramagnetic behavior with very weak antiferromagnetic interactions between the Tb^{3+} spins in the glass structure.

In order to determine the effective magnetic moment, μ_{eff} , per rare earth ion, at first a diamagnetic correction was done based on the experimental data obtained on the undoped glass. The Curie constant can be obtained from the inverse of the slope in the inset of Fig. 7a-b, by using Eq. (3):

$$\mu_{\text{eff}} = \sqrt{\frac{3k_B C}{N_A}} = 2.83\mu_B \sqrt{C/\Delta} \quad (3)$$

where k_B is the Boltzmann's constant, N_A is the Avogadro's number, and μ_B is the Bohr magneton and where Δ is the terbium content in mole cm^{-3} .

As shown in Fig. 7a-b, the results of glasses with 3 and 10 mol% of Tb ions are well described by the Curie–Weiss law in the whole range of temperatures. For lower concentration of Tb ions, the fit provides Weiss temperatures of $\theta(\text{FC}) = -1.06$ K and $\theta(\text{ZFC}) = -0.904$ K, suggesting the occurrence of weak antiferromagnetic interactions between the rare-earth ions, and $C(\text{FC}) = 44.36$ emu K mol^{-1} and $C(\text{ZFC}) = 42.78$ emu K mol^{-1} . In our study, neither a blocking temperature nor a significant difference between ZFC and FC measurements were observed for the samples. This indicates that our glasses are not superparamagnetic materials, which is a strong evidence that magnetic clusters are not formed, corroborating the TEM and EXAFS results [73–75]. The

effective magnetic moment per rare earth ion is found to be $9.43 \mu_B$ for FC measurements and $9.25 \mu_B$ for ZFC measurements. The calculated effective magnetic moment for Tb^{3+} ions is slightly lower than the theoretical value ($9.72 \mu_B/\text{Tb}^{3+}$ ion) while, the negative value of θ indicates weak antiferromagnetic interactions. A similar analysis carried out for the sample with 10 mol% of Tb_4O_7 (see Fig. 7c-d) yields Weiss temperature of $\theta(\text{FC}) = -1.09$ K, and $\theta(\text{ZFC}) = -0.869$ K, which indicates also an antiferromagnetic interaction between rare-earth ions. For the Curie constants we obtain $C(\text{FC}) = 43.87$ emu K mol^{-1} and $\theta(\text{ZFC}) = 42.90$ emu K mol^{-1} . The effective magnetic moment per rare earth ion is found to be $9.37 \mu_B$ for FC and $9.27 \mu_B$ for ZFC measurements.

Additional information on the specific magnetic behaviour of the magnetic glasses comes from isothermal magnetization measurements as a function of the applied magnetic field. Fig. 7c and 7d shows this data as a function of Tb concentration, both at 5 and at 300 K. As can be seen, no hysteresis loop was observed for any of the six samples. It is clear that the magnetization of the doped samples at 5 K tends to saturate above 30 kOe. The data are well described by the Brillouin function (Eqs. (4) and (5)),

$$M = n g J \mu_B B_J(x) \quad (4)$$

where

$$B_J(x) = \left[\frac{(2J+1)}{2J} \right] \coth \left[\frac{(2J+1)x}{2J} \right] - \left[\frac{1}{2J} \right] \coth \left[\frac{x}{2J} \right] \quad (5)$$

here M is the molar magnetization, n is the number of magnetic ions per unit mass, $\coth(x)$ is the hyperbolic cotangent function, J is the total angular momentum quantum number of Tb^{3+} ($J = 6$) and $x = g \mu_B H / (k_B T)$. The best fit using equation (3) is shown in the inset of Fig. 7c-d and in the Fig. SM6a-b, SM7a-b and SM8a-b for both temperatures 300 K and 5 K.

5.2. Faraday rotation of the bulk glasses

The Verdet constant V_B characterizes the intrinsic ability of a material to rotate the plane of light polarization upon application of a magnetic field in the propagation direction of light [9,29]. It is determined by measuring the rotation angle θ (in rad) obtained for an optical path length l (in m) at a given magnetic flux density (in T), according to Eq. (6). Its sign is positive for diamagnetic materials and negative for paramagnetic materials [29]. The wavelength dependence of V_B is given by Van Vleck-Hebb (Eq. (7)):

$$\theta = V_B \cdot B \cdot l \quad (6)$$

$$V_B^{-1} = \frac{g \mu_B c h}{4 \pi^2 \chi C_t} \left(1 - \frac{\lambda^2}{\lambda_t^2} \right) \quad (7)$$

where g is the Landé factor, c the speed of light, μ_B the Bohr magneton, h is the Planck constant, χ is the volume magnetic susceptibility, and C_t the effective transition probability relating to the wavelength λ_t^2 of the closest optical $4f^n \rightarrow 4f^{n-1} 5d^1$ transition [29]. Eq. (6) predicts large Verdet constants for glasses with large paramagnetic susceptibilities and high optical transition probability, which is the case for glasses containing high concentrations of Tb^{3+} [9].

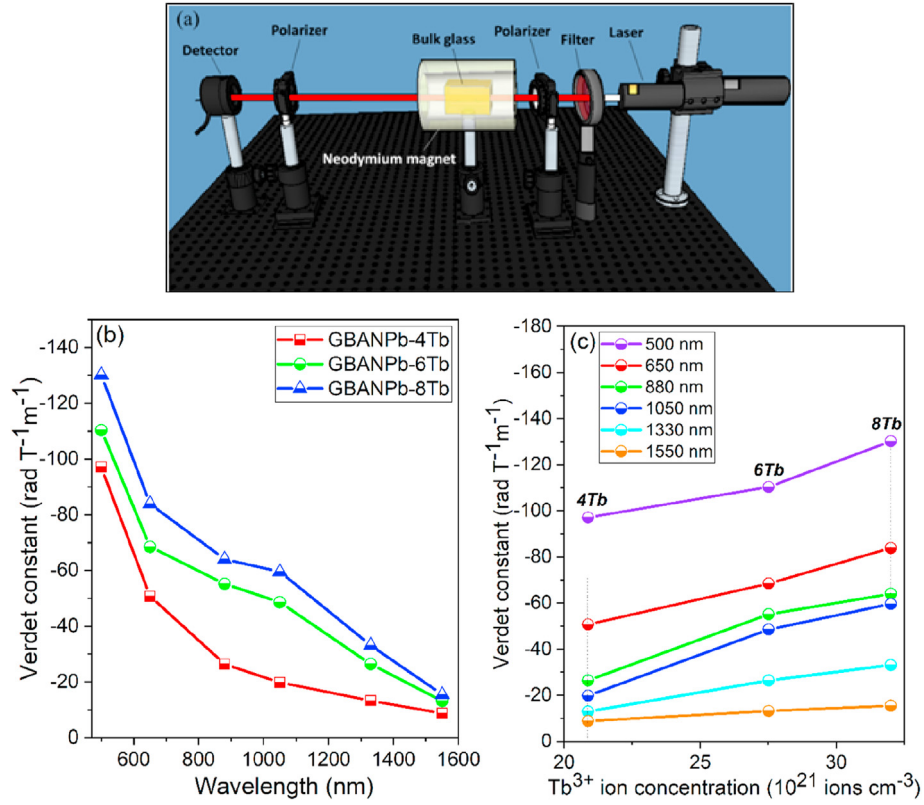


Fig. 8 – (a) Schematic illustration of the setup used to measure the V_B values of GBANPb- x Tb samples ($x = 4, 6$ and 8 mol% of Tb_4O_7), (b) Verdet constant values as a function of wavelength and (c) as a function of the Tb^{3+} content.

Fig. 8a shows the schematic illustration of the setup used to measure the V_B values of GBANPb- x Tb samples ($x = 4, 6$ and 8 mol% of Tb_4O_7). Fig. 8b shows the V_B values obtained at different wavelengths.

Fig. 8c plots the V_B values for the GBANPb- x Tb glasses as a function of Tb^{3+} density, calculated from Eq. (8) [76].

$$N_{Tb} \text{ (ions cm}^{-3}\text{)} = \frac{4x\rho N_A}{M} \quad (8)$$

where x is the mole fraction of Tb_4O_7 , ρ is the density of GBANPb- x Tb glasses, N_A is Avogadro's constant and M is the average molecular weight of the glass. We observe the

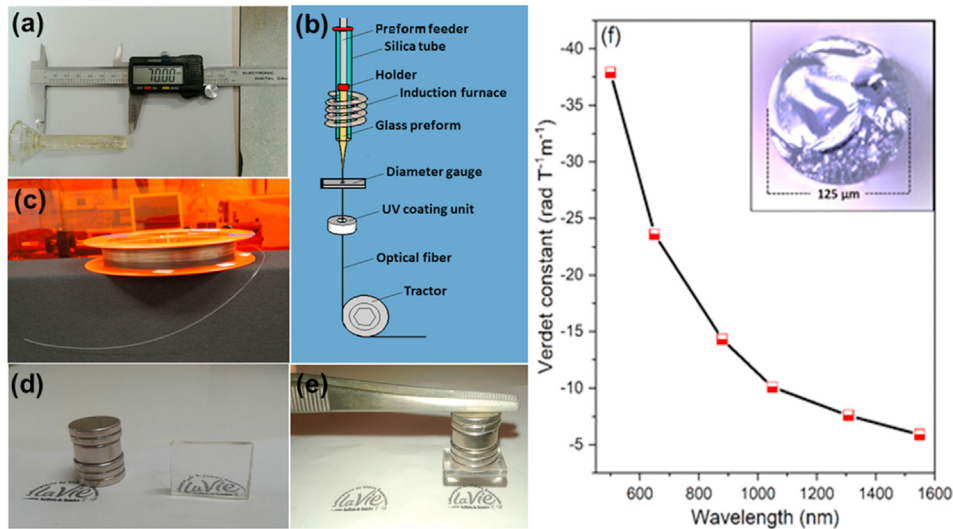


Fig. 9 – (a) Glass preform (b) Scheme for optical fiber drawing. (c) GBANPb-4Tb magneto-optical glass fiber; (c) Preform (d) GBANPb-4Tb₄O₇ glass piece (e) GBANPb-4Tb₄O₇ magneto-optical glass being attracted by Nd-magnet and (f) Verdet constant as a function of the wavelength for the GBANPb-4Tb fiber. Inset – Optical image cross section of the magneto-optical fiber.

Table 4 – Verdet constant (V_B) values of RE-doped silica fibers compared with the Terbium-doped borogermanate fiber at 650, 1050 and 1550 nm.

Magneto-optical fibers	Verdet constant ($\text{rad T}^{-1} \text{m}^{-1}$)			References
	650/660 nm	1053 nm	1550 nm	
SMF (commercial)	2.413 (at 660 nm)	1.2	0.589	[37,41]
Eu ³⁺ -doped silica	−4.564 (at 660 nm)	–	−0.619	[83]
Er ³⁺ -doped silica (EDF)	−3.379 (at 660 nm)	–	−0.619	[83]
Ho ³⁺ -doped silica	–	–	−1.287	[94]
GBANPb-4Tb	−23.6 (at 650 nm)	−10.5 (at 1050 nm)	−5.89	(This Work)
Pr ³⁺ -aluminosilicate fiber	−17.28 (at 650 nm)	–	–	[95]
65 wt% Tb ³⁺ -doped	–	−32.1	–	[81]
56 wt% Tb ³⁺ -doped	–	−24.5	–	[37]
Gd ₂ O ₃ NPs-doped	−3.18 (at 650 nm)	–	–	[80]

expected linear dependence of the V_B values on the Tb³⁺ concentration (density of Tb³⁺ ions per volume of glass in cm^{-3}), as previously observed for other glass systems [4,9,18,77–79].

As shown in Fig. 9b, GBANPb-8Tb glass presents V_B values of −59.6, −33.2 and −15.5 $\text{rad T}^{-1} \text{m}^{-1}$ at 1.05, 1.33 and 1.55 μm , respectively. While these numbers are lower than the highest values previously reported in the literature, it is important to point out here, that the goal of the present study was to develop magneto-optical glasses with sufficient stability for fiber drawing. As discussed below, with respect to the latter criterion, the present glass system has the best characteristics known to date.

6. Magneto-optical fiber and Faraday rotation measurements

Magneto-optical fibers offer the opportunity of enhancing the rotation angle by employing significantly longer path lengths than possible with bulk samples. Compared to conventionally used magneto-optic (diamagnetic) silica fiber [80–82,86,87,93], rare-earth doped glass fibers present significantly larger Verdet constant owing to their large magnetic susceptibilities. Among the rare-earth ions, Tb³⁺ has been the most favorable candidate because of this optical absorption behavior [80,81,83–85]. According to Gao et al. [9] and Yamani and Asahara [29] the values of V_B for different families of Tb-containing magneto-optical glasses increase at fixed Tb content in the order of phosphate [90], aluminum-silicate [91] and borogermanate glasses [92].

As discussed before in relation to the DSC data, the stability parameter (ΔT) for all the glasses analyzed here is around 200 °C, conferring them enough stability against devitrification during the drawing process. We selected the glass with the highest stability ($\Delta T = 290$ °C), GBANPb-4Tb for our fiber drawing experiments. A glass rod measuring 70 mm in length and 10 mm in diameter, was prepared as shown in Fig. 9a. Fig. 9b shows the schematic of the fiber drawing process while Fig. 9c shows the obtained optical fiber of composition GBANPb-4Tb in perspective.

Fig. 9d shows the Verdet constants for the GBANPb-4Tb fiber (~21.4 wt% of Tb-dopant) as a function of wavelength.

Table 4 compares these values with those reported to date in the literature for glass fibers at 650, 1050, and 1550 nm. The V_B values measured at 500 and 650 nm (−37.9 and −23.6 $\text{rad T}^{-1} \text{m}^{-1}$, respectively) belong to the highest ones reported to date on a glass fiber. A slightly higher value (−28 $\text{rad T}^{-1} \text{m}^{-1}$) was reported by Shiyu et al. for tellurite glass fiber at 633 nm [88]. At 1050 nm our glass reaches a Verdet constant of −10.1 $\text{rad T}^{-1} \text{m}^{-1}$, i.e. approximately eight times higher than that of conventional silica fiber ($V_B \sim 1.2$ $\text{rad T}^{-1} \text{m}^{-1}$) [37,41]. It also exceeds the value −6.2 $\text{rad T}^{-1} \text{m}^{-1}$ at 1053 nm [84] in phosphate-based materials whereas it is lower than the values of −32 $\text{rad T}^{-1} \text{m}^{-1}$ and −24 $\text{rad T}^{-1} \text{m}^{-1}$ measured on silicate fibers containing 65 and 56 wt%-terbium ions [81,84], respectively for 56 wt.% Tb-doped silicate fiber [83,89]. Finally, the V_B value for the GBANPb-4Tb fiber at 1550 nm (−5.89 $\text{rad T}^{-1} \text{m}^{-1}$) is the highest one ever reported to date, and found ten times larger than that of commercial SMF fiber.

7. Conclusion

In summary, we have reported the synthesis of transparent new Tb³⁺-borogermanate magneto optical glasses and comprehensively characterized its thermal, structural, magnetic and optical properties. These glasses are free of nanocrystals and show strong paramagnetism with very weak local antiferromagnetic interactions. The high thermal stability parameter (>200 °C) and the absence of crystals, allowed the preparation of magneto-optical glass fibers with good quality. The Verdet constant values were experimentally measured for bulk glasses and optical fiber in the visible and near infrared regions. The V_B values of magneto-optical fibers fabricated from GBANPb glass containing 4 mol% Tb₄O₇ characterize this material as one of the best Faraday rotator fibers with application potential in telecommunication systems.

Declaration of Competing Interest

The authors declare that they have no known competing financial interests or personal relationships that could have appeared to influence the work reported in this paper.

Acknowledgments

The authors are grateful to the Brazilian Agency São Paulo Research Foundation (FAPESP) grant numbers (2016/16900-9, 2018/19272-4 and 2013/07793-6) for the financial support, to the Centre d'Optique, Photonique et laser (COPL) at Laval University – Canada and LNLS (Brazilian synchrotron facilities) for XAS measurements.

Appendix A. Supplementary data

Supplementary data to this article can be found online at <https://doi.org/10.1016/j.jmrt.2021.01.010>.

REFERENCES

- [1] Stookey SD. *Proc Inst Electr Eng* 1966;113:1151–8.
- [2] Hench LL. The story of Bioglass. *J Mater Sci Mater Med* 2006;17:967–78.
- [3] Marjanovic S, Nieber AR, Piech GA, Schillinger H, Tsuda S, Wagner RS. Corning Incorporated. Laser cutting of displays glass compositions. US20150232369A1, United States, Patent, 20 August 2015.
- [4] Mo ZX, Guo HW, Liu P, Shen YD, Gao DN. Luminescence properties of magneto-optical glasses containing Tb³⁺ ions. *J Alloys Compd* 2016;658:967–72.
- [5] Valeanu M, Sofraïne M, Galca AC, Tolea F, Elisa M, Sava B, et al. The relationship between magnetism and magneto-optical effects in rare earth doped aluminophosphate glasses. *J Phys D Appl Phys* 2016;49:75001.
- [6] Golis E. The effect of Nd³⁺ impurities on the magneto-optical properties of TeO₂–P₂O₅–ZnO–LiNbO₃ tellurite glass. *RSC Adv* 2016;6:22370–3.
- [7] Shen Y, Lu Y, Yu X, Liu Z, Zhang G, Yu W. Characteristics of rare-earth-doped glass in optical current transducers. *Optik* 2016;127:2069–73.
- [8] Chen Q, Wang H, Chen Q. Structural and properties of heavy metal oxide Faraday glass for optical current transducer. *J Non-Cryst Solids* 2015;429:13–9.
- [9] Gao G, Winterstein-Beckmann A, Surzhenko O, Dubs C, Dellith J, Schmidt MA, et al. Faraday rotation and photoluminescence in heavily Tb³⁺-doped GeO₂–B₂O₃–Al₂O₃–Ga₂O₃ glasses for fiber-integrated magneto-optics. *Sci Rep* 2015;5:1–6.
- [10] Guo H, Wang Y, Gong Y, Yin H, Mo Z, Tang Y, et al. Optical band gap and photoluminescence in heavily Tb³⁺ doped GeO₂–B₂O₃–SiO₂–Ga₂O₃ magneto-optical glasses. *J Alloys Compd* 2016;686:635–40.
- [11] Urdampilleta M, Klyatskaya S, Ruben M, Wernsdorfer W. Landau-Zener. Tunneling of a single Tb³⁺ magnetic moment allowing the electronic read-out of a nuclear spin. *Phys Rev B* 2013;87:195412.
- [12] Lin H, Wang X, Lin L, Li C, Yang D, Tanabe S. Near-infrared emission character of Tm³⁺-doped heavy metal tellurite glasses for optical amplifiers and 1.8 μm infrared laser. *J Phys D Appl Phys* 2007;40:3567–72.
- [13] Kumar M, Rajesh D, Balakrishna A, Ratnakaram YC. Optical absorption and photoluminescence properties of Dy³⁺ doped heavy metal borate glasses – effect of modifier oxides. *J Mol Struct* 2013;1041:100–5.
- [14] Tang B, Wu C, Li J, Fan Y, Hu H, Zhang L. Large-size oxyfluoride glasses used for Vis–IR-transmitting windows. *J Non-Cryst Solids* 2009;355:2006–9.
- [15] Ivanov AO, Evstropiev KS. On the question of simple germanate. *Dokl Akad Nauk SSSR* 1962;145:797–800.
- [16] Henderson GS, Neuville DR, Cochain B, Cormier L. The structure of GeO₂–SiO₂ glasses and melts: a Raman spectroscopy study. *J Non-Cryst Solids* 2009;355:468–74.
- [17] Qiu J, Tanaka K, Sugimoto N, Hirao K. Faraday effect in Tb³⁺-containing borate fluoride and fluorophosphate glasses. *J Non-Cryst Solids* 1997;213–214:93–198.
- [18] Yin H, Gao Y, Gong Y, Buchanan R, Song J, Li M. Wavelength dependence of Tb³⁺ doped magneto-optical glass Verdet constant. *Ceram Int* 2018;44:10929–33.
- [19] Hayakawa T, Nogami M, Nishi N, Sawanobori N. Faraday rotation effect of highly Tb₂O₃/Dy₂O₃-concentrated B₂O₃–Ga₂O₃–SiO₂–P₂O₅ glasses. *Chem Mater* 2002;14:3223–5.
- [20] Suzuki F, Sato F, Oshita H, Yao S, Nakatsuka Y, Tanaka K. Large Faraday effect of borate glasses with high Tb³⁺ content prepared by containerless processing. *Opt Mater* 2018;76:174–7.
- [21] Hao D, Chen J, Ao G, Tian YT, Tang Y, Yi X, et al. Effect of Tb₄O₇ excess on the microstructure and magneto-optical properties of TAG transparent ceramic. *Opt Mater* 2019;94:47–52.
- [22] Jin W, Gai L, Chen J, Lin H, Li C, Su L, et al. Fabrication and magneto-optical properties of TGG transparent ceramics. *Phys B Condens Matter* 2019;555:96–8.
- [23] Geho M, Sekijima T, Fujii T. Development of optical isolators for visible light using terbium aluminum garnet (Tb₃Al₅O₁₂) single crystals. *J Cryst Growth* 2004;267:188–93.
- [24] Jin W, Ding J, Guo L, Gu Q, Li C, Su L, et al. Growth and performance research of Tb₃Ga₅O₁₂ magneto-optical crystal. *J Cryst Growth* 2018;484:17–20.
- [25] Chen Q. WO₃ concentration-dependent magneto-optical properties of Faraday rotating glasses and glass-ceramics. *J Non-Cryst Solids* 2019;522:119584.
- [26] Balabanov SS, Permin DA, Rostokina EY, Palashov OV, Snetkov IL. Characterizations of REE: Tb₂O₃ magneto-optical ceramics. *Phys Status Solidi B* 2019;1900474:1–7.
- [27] Dai J, Snetkov IL, Palashov OV, Pan Y, Kou H, Li J. Fabrication, microstructure and magneto-optical properties of Tb₃Al₅O₁₂ transparent ceramics. *Opt Mater* 2016;62:205:210.
- [28] Chen Q, Wang H, Wang Q, Chen Q. Faraday rotation influence factors in tellurite-based glass and fibers. *Appl Phys A-Mater* 2015;120:1001–10.
- [29] Yamane M, Asahara Y. *Glasses for photonics*. 1st ed., vol. 1. Cambridge: Univ. Press; 2000. p. 241–63.
- [30] Ambekar JD, Panmand RP, Sonawane RS, Apte SK, Hundiware DG, Kale BB. Preparation and magneto-optical properties of stable bismuth phosphate nanoparticles in phosphate glass. *RSC Adv* 2015;5:48112–7.
- [31] De Oliveira Jr M, Amjad RJ, De Camargo ASS, Eckert H. Network former mixing effects in heavy metal oxide glasses: structural characterization of lead zinc phosphotellurite glasses using NMR and EPR spectroscopies. *J Phys Chem C* 2018;122:23698–711.
- [32] Schmidt MA, Wondraczek L, Lee HW, Granzow N, Da N, Russel PS. Complex Faraday rotation in microstructured magneto-optical fiber waveguides. *J Adv Mater* 2011;23:2681–8.
- [33] Bernal ME, Dussan A, Mesa F. Structural, optical and morphological properties of Ga_{1-x}Mn_xAs thin films deposited by magnetron sputtering for spintronic device applications. *Phys B Condens Matter* 2012;407:3210–3.

- [34] Pedroso CB, Munin E, Villaverde AB, Neto JAM, Aranha N, Barbosa LC. Magneto-optical rotation of heavy-metal oxide glasses. *Opt Eng* 1998;38:214–9.
- [35] Yin H, Gao Y, Guo H, Wang C, Yang C. Effect of B_2O_3 content and microstructure on Verdet constant of Tb_2O_3 -doped GBSG magneto-optical glass. *J Phys Chem C* 2018;122:16894–900.
- [36] Day GW, Payne DN, Barlow AJ, Ramskov-Hansen JJ. Faraday rotation in coiled, monomode optical fibers: isolators, filters, and magnetic sensors. *Opt Lett* 1982;7:238–40.
- [37] Sun L, Jiang S, Zuegel JD, Marcianite JR. All-fiber optical isolator based on Faraday rotation in highly terbium-doped fiber. *Opt Lett* 2010;35:706–8.
- [38] Turner EH, Stolen RH. Fiber Faraday circulator or isolator. *Opt Lett* 1981;6:322–3.
- [39] Cheng L, Han J, Guo Z, Jin L, Guan BO. Faraday-rotation-based miniature magnetic field sensor using polarimetric heterodyning fiber grating laser. *Opt Lett* 2013;38:688–90.
- [40] Ballato J, Snitzer E. Fabrication of fibers with high rare-earth concentrations for Faraday isolator applications. *Appl Optic* 1995;34:6848–54.
- [41] Cruz JL, Andres MV, Hernandez MA. Faraday effect in standard optical fibers: dispersion of the effective Verdet constant. *Appl Optic* 1996;35:922–7.
- [42] Bellanger B, Ledemi Y, Messaddeq Y. Fluorophosphate glasses with high terbium content for magneto-optical applications. *J Phys Chem C* 2020;124:5353–62.
- [43] Michalowicz A, Moscovici J, Muller-Bouvet D, Provost K. MAX: Multiplatform applications for XAFS. *J Phys Conf Ser* 2009;190:12034.
- [44] Ankudinov AL, Ravel B, Rehr JJ, Conradson SD. Real-space multiple-scattering calculation and interpretation of x-ray-absorption near-edge structure. *Phys Rev B Condens Matter* 1998;58:7565–76.
- [45] Yamashita T. Concentration and temperature effects on the spectroscopic properties of Tb^{3+} doped borosilicate glasses. *J Appl Phys* 2007;102:123107.
- [46] Potdevin A, Chadeyron G, Briois V, Leroux F, Mahiou R. Modifications involved by acetylacetone in properties of sol-gel derived $Y_3Al_5O_{12}:Tb^{3+}$ – II: optical features. *Dalton Trans* 2010;39:8718–24.
- [47] Witkowska A, Sikora B, Trzebiatowski K, Rybicki J. Germanate anomaly in heavy metal oxide glasses: an EXAFS analysis. *J Non-Cryst Solids* 2006;352:4356–61.
- [48] Rada M, Aldea N, Wu ZH, Jing Z, Rada S, Culea E, et al. Evolution of the germanium-oxygen coordination number in lithium-lead-germanate glasses. *J Non-Cryst Solids* 2016;437:10–6.
- [49] Bowron DT, Newport RJ, Rainford BD, Saunders GA, Senin HB. EXAFS and x-ray structural studies of $(Tb_2O_3)_{0.26}(P_2O_5)_{0.74}$ metaphosphate glass. *Phys Rev B Condens Mater* 1995;51:5739.
- [50] Bowron DT, Saunders GA, Newport RJ, Rainford BD, Senin HB. EXAFS studies of rare-earth metaphosphate glasses. *Phys Rev B Condens Matter* 1996;53:5268–75.
- [51] Ribeiro SJL, Dexpert-Ghys J, Piriou B, Mastelaro VR. Structural studies in lead germanate glasses: EXAFS and vibrational spectroscopy. *J Non-Cryst Solids* 1993;159:213–21.
- [52] Koroleva ON, Shtenberg MV, Zainullina RT, Lebedeva SM, Nevolina LA. Vibrational spectroscopy and density of $K_2O-B_2O_3-GeO_2$ glasses with variable B/Ge ratio. *Phys Chem Chem Phys* 2019;21:12676–84.
- [53] Knoblochova K, Ticha H, Schwarz J, Tichy L. Raman spectra and optical properties of selected $Bi_2O_3-PbO-B_2O_3-GeO_2$ glasses. *Opt Mater* 2009;31:895–8.
- [54] Mansour E. Raman spectra and density of $Li_2O-B_2O_3-GeO_2$ glasses with high Li_2O content. *Phys B Condens Matter* 2010;405:281–6.
- [55] Alvarado-Rivera J, Rodríguez-Carvajal DA, Acosta-Enríquez MC, Manzanara-Martínez MB, Alvarez E, Lozada-Morales R, et al. Effect of CeO_2 on the glass structure of sodium germanate glasses. *J Am Ceram Soc* 2014;97:3494–500.
- [56] Di Martino D, Santos LF, Marques AC, Almeida RM. Vibrational spectra and structure of alkali germanate glasses. *J Non-Cryst Solids* 2001;293–295:394–401.
- [57] Henderson GS, Fleet ME. The structure of glasses along the Na_2O-GeO_2 join. *J Non-Cryst Solids* 1991;134:259–69.
- [58] Micoulaut M, Cormier L, Henderson GS. The structure of amorphous, crystalline and liquid GeO_2 . *J Condens Matter Phys* 2006;18:R753.
- [59] Kamitsos EI, Yiannopoulos YD, Karakassides MA, Chrysos GD, Jain H. Raman and infrared structural investigation of $xRb_2O \cdot (1-x)GeO_2$ glasses. *J Phys Chem* 1996;100:11755–65.
- [60] Kamitsos EI, Chrysos GD. Borate glass structure by Raman and infrared spectroscopies. *J Mol Struct* 1991;247:1–16.
- [61] Yadav AK, Singh P. A review of the structures of oxide glasses by Raman spectroscopy. *RSC Adv* 2015;5:67583–609.
- [62] Hubert M, Faber AJ. On the structural role of boron in borosilicate glasses. *Phys Chem Glasses* 2014;55:136–58.
- [63] Henderson GS, Soltay LG, Wang HM. Q speciation in alkali germanate glasses. *J Non-Cryst Solids* 2010;356:2480–5.
- [64] Koroleva ON, Shtenberg MV, Ivanova TN. The structure of potassium germanate glasses as revealed by Raman and IR spectroscopy. *J Non-Cryst Solids* 2019;510:143–50.
- [65] Ravangave LS, Devde GN. Structure and physical properties of $59B_2O_3-10Na_2O-(30-x)CdO-xZnO-1CuO$ ($0 \leq x \leq 30$) glass system. *Adv in Glass Sci and Technol* 2018;2:21–38.
- [66] Chrysos GD, Kamitsos EI. A Raman investigation of cadmium borate and borogermanate glasses. *J Non-Cryst Solids* 1987;93:155–68.
- [67] Osipov AA, Osipova LM. Structural studies of $Na_2O-B_2O_3$ glasses and melts using high-temperature Raman spectroscopy. *Phys B Condens Matter* 2010;405:4718–32.
- [68] Ameh ES. A review of basic crystallography and x-ray diffraction applications. *Int J Adv Manuf Technol* 2019;105:3289–302.
- [69] Rachkovskaya GE, Zakharevich GB. Germanate lead-tellurite glasses for optical light filters. *Glass Ceram* 2012;68:385–8.
- [70] Wan X, Zhong Q, Tie S, Shen J. Synthesis and luminescence properties of Tb^{3+} activated $CaO-Al_2O_3-B_2O_3$ glass. *Optoelectron Adv Mat* 2011;5:538–44.
- [71] Linganna K, Ju S, Basavapoornima Ch, Venkatramu V, Jayasankar CK. Luminescence and decay characteristics of Tb^{3+} -doped fluorophosphate glasses. *J Asian Ceram Soc* 2018;6:82–7.
- [72] Suthanthirakumar P, Mariyappan M, Marimuthu K. Spectroscopic investigations on Pr^{3+} ions doped lead telluroborate glasses for photonic applications. *AIP Conf Proc* 1942;2018:70004.
- [73] Hayakawa T, Sato K, Yamada K, Kamata N, Nishi N, Maruyama F. Lifetime for $^5D_4 \rightarrow ^7F_5$ emission in heavily Tb^{3+} -doped superparamagnetic glasses. *Synth Met* 1997;91:355–6.
- [74] Karabulut M, Popa A, Berghian-Grosan C, Ertap H, Yüsek M, Öztürk ST, et al. On the structural features of iron-phosphate glasses by Raman and EPR: observation of superparamagnetic behavior differences in HfO_2 or CeO_2 containing glasses. *J Mol Struct* 2019;1191:59–65.
- [75] Shen TD, Schwarz RB, Thompson JD. Paramagnetism, superparamagnetism, and spin-glass behavior in bulk amorphous $Pd-Ni-Fe-P$ alloys. *J Appl Phys* 1999;85:4110.
- [76] Mohan S, Thind KS, Sharma G. Effect of Nd^{3+} concentration on the physical and absorption properties of sodium-lead-borate glasses. *Braz J Phys* 2007;37:1306–13.

- [77] Chen Q, Chen Q, Wang H, Wang G, Yin S. Magneto optical properties of rare earth Tb_2O_3 doped $\text{PbO-Bi}_2\text{O}_3\text{-B}_2\text{O}_3$ glass. *J Non-Cryst Solids* 2017;470:99–107.
- [78] Malshakov AN, Pasmanik GA, Potemkin AK. Comparative characteristics of magneto-optical materials. *Appl Optic* 1997;36:6403–10.
- [79] Kumari S, Chakraborty S. Study of different magneto-optic materials for current sensing applications. *J Sens Sens Syst* 2018;7:421–31.
- [80] Ju S, Kim J, Linganna K, Watekar PR, Kang SG, Kim BH, et al. Temperature and vibration dependence of the Faraday effect of Gd_2O_3 NPs-doped aluminosilicate glass optical fiber. *Sensors* 2018;18:988.
- [81] Sun L, Jiang S, Marciante JR. Compact all-fiber optical Faraday components using 65-wt%-terbium-doped fiber with a record Verdet constant of $-32 \text{ rad}/(\text{T.m})$. *Optic Express* 2010;18:12191–6.
- [82] Annovazzi-Lodi V, Donati S, Merlo S, Leona A. All-fiber Faraday rotator made by a multiturn figure-of-eight coil with matched birefringence. *J Lightwave Technol* 1995;13:2349–53.
- [83] Huang Y, Chen H, Dong W, Pang F, Wen J, Chen Z, et al. Fabrication of europium-doped silica optical fiber with high Verdet constant. *Optic Express* 2016;24:18709–17.
- [84] Sun L, Jiang S, Zuegel JD, Marciante JR. Effective Verdet constant in a terbium-doped-core phosphate fiber. *Opt Letters* 2009;34:1699–701.
- [85] Valiev UV, Zvezdin AK, Krinchik GS, Levitin RZ, Mukimov KM, Popov AI. Faraday effect of rare-earth iron garnets in strong magnetic fields. *J Exp Theor Phys* 1983;58:181–9.
- [86] Smith AM. Polarization and magneto optic properties of single-mode optical fiber. *Appl Optic* 1978;17:52–6.
- [87] Smith AM. Faraday effect in single-mode optical fibre using an injection laser light source. *Electron Lett* 1980;16:206–8.
- [88] Shiyu Y, Lousteau J, Olivero M, Merlo M, Boetti N, Abrate S, et al. Analysis of Faraday effect in multimode tellurite glass optical fiber for magneto-optical sensing and monitoring applications. *Appl Optic* 2012;51:4542–6.
- [89] Kim Y, Ju S, Jeong S, Jang MJ, Kim JY, Lee NH, et al. Influence of gamma-ray irradiation on Faraday effect of Cu-doped germano-silicate optical fiber. *Nucl Instrum Methods Phys Res B* 2015;344:39–43.
- [90] Babkina A, Fedorov Y, Aseev V, Sobolev D. Terbium-doped phosphate glass for Faraday isolators. In: *International conference laser optics (ICLO)*; 2018. 213–213.
- [91] Robinson CC, Graf RE. Faraday rotation in praseodymium, terbium, and dysprosium alumina silicate glasses. *Appl Optic* 1964;3:1190–1.
- [92] Savinkov VI, Sigaev VN, Golubev NV, Sarkisov PD, Masalov AV, Sergeev AP. Borogermanate glasses with a high terbium oxide content. *J Non-Cryst Solids* 2010;356:1655–9.
- [93] Asraf S, Sintov Y, Zalevsky Z. Novel configuration for an enhanced and compact all-fiber Faraday rotator with matched birefringence. *Optic Express* 2017;25:18643–55.
- [94] Liu Z, Chen Z, Chen N, Huang Y, Liu S, Shang Y, et al. Study of the Verdet constant of the holmium-doped silica fiber. *OSA Continuum* 2020;3:1096–104.
- [95] Linganna K, Ju S, Lee Y, Han WT. Development of aluminosilicate glass fiber doped with high Pr^{3+} concentration for all-optical fiber isolator application. *J Mater Sc: Mater Electron* 2019;30:12790–5.